Contract No.:

This manuscript has been authored by Savannah River Nuclear Solutions (SRNS), LLC under Contract No. DE-AC09-08SR22470 with the U.S. Department of Energy (DOE) Office of Environmental Management (EM).

Disclaimer:

The United States Government retains and the publisher, by accepting this article for publication, acknowledges that the United States Government retains a non-exclusive, paid-up, irrevocable, worldwide license to publish or reproduce the published form of this work, or allow others to do so, for United States Government purposes.

X-ray topographic study of Bridgman-grown CdZnTeSe

Utpal N. Roy[1*†], Giuseppe S. Camarda[1], Yonggang Cui[1] and Ralph B. James[1*]

[1]Brookhaven National Laboratory, Upton, NY 11973, USA.
[*]Present address: Savannah River National Laboratory, Aiken, SC 29808, USA.

Abstract:

We have characterized the structural quality of $Cd_{0.9}Zn_{0.1}Te_{0.93}Se_{0.07}$ ingot grown by the vertical Bridgman growth technique. The structural quality of $Cd_{0.9}Zn_{0.1}Te_{0.93}Se_{0.07}$ ingot along the length was investigated via X-ray topography in the reflection mode using a white beam synchrotron radiation source. The X-ray topography data revealed the presence of very few sub grain boundaries and no sub-grain boundary network for the CdZnTeSe samples used in this study.

[†]Corresponding author: Utpal.Roy@srnl.doe.gov.

1. Introduction

The II-VI ternary compound $Cd_{0.9}Zn_{0.1}Te$ (CZT) has been the material of choice for over three decades for X- and gamma-ray detectors operating at room temperature. In general, since gamma-ray detectors demand large thicknesses as compared to most optical detectors to absorb the incident photons, the material requirements are more stringent for devices that work in the charge-collection mode. The ideal material for fabricating a gamma-ray detector should possess high atomic numbers for the elements to stop the gammas and a large band gap to enable high resistivity at room temperature to minimize noise attributed to the leakage current. To realize detectors with a thickness of 1 cm or greater, the material requires excellent charge transport properties. CZT meets these requirements for some niche gamma detector applications, but broader applicability is desired [1-5]. Despite a continuing global search for an alternative material, CZT and CdTe are still the only successful high-resolution semiconductor materials available commercially for gamma- and X-ray spectroscopy. Over the past few years, the quality of CZT has improved considerably with reduced cost; however, widespread deployment remains elusive due to the presence of performance-limiting structural defects such as sub-grain boundary networks and secondary phases usually composed of Te inclusions [6-9]. These defects act as electron trapping centers and severely hamper the charge-transport characteristics of the material [9, 10]. The sub-grain boundary networks are often found to be randomly distributed in the CZT matrix, and the sub-grain boundaries are also known to be decorated with Te inclusions [11, 12]. Sub-grain boundaries are the dislocation walls, where high concentration of dislocations are arranged along the planes [11,13]. It has been demonstrated that the mobility-lifetime product for electrons [$(\mu\tau)_e$] in CZT can vary over a large range of between 0.2 and $20\text{x}10^{-3}$ cm^2/V for the regions with Te inclusions compared to the clear regions that are relatively free from large

inclusions [14]. Furthermore, the non-uniform distribution of these defects in the CZT matrix induces a spatial non-uniformity in the charge-transport properties in the device and eventually severely degrades the device performance as the detector thickness grows or the applied voltage bias decreases [15]. The spatial non-uniformity of the charge-transport properties due to the non-uniform distribution of defects with a sub-grain boundary network in the CZT matrix is perhaps the dominant reason for the degradation of device performance. In addition, it severely hinders the yield of high-quality detector grade material. The sub-grain boundaries and their network cannot be removed by post-growth annealing; however, eliminating the Te inclusions from the CZT matrix by post-growth annealing is a common processing step in CZT detector manufacturing. Unfortunately, the process is known to produce large star-like defects in the post-annealed matrix. They are invisible in an IR transmission mode, but they are detectable by charge collection and etch-pit density measurements. Depending on their concentration and size, these star-like defects can severely hamper the charge-transport properties [16] and the device performance [17]. Thus, producing material with reduced or even zero sub-grain boundaries is expected to increase the performance and yield of high-quality detectors.

Selenium, when added to CdTe and CdZnTe matrices, has been reported to be very effective for solution hardening to reduce the cellular structure or sub-grain boundaries and lower the dislocation density [18, 19]. In the recent past, we observed the efficacy of adding Se in the CdTe matrix as an alternative detector material. The resultant ternary CdTeSe (CTS) compound was free from sub-grain boundary networks and showed reduced Te inclusions [20, 21]. Fiederle *et al*. reported higher charge collection efficiency for CTS as compared to CdTe and CZT [22]. In other words, the partial substitution of Te with Se in CdTe and in CdZnTe matrices improves the material quality and charge collection and demonstrated an increased homogeneity of the

electrical properties [18-22]. Our recent results showed the quaternary material CdZnTeSe with concentrations of 10% Zn and 2% Se or of 10% Zn and 7% Se, when grown using the THM technique, were free from sub-grain boundary networks [23-25].

In this paper we report the results of an X-ray topographic study of Bridgman-grown $Cd_{0.9}Zn_{0.1}Te_{0.93}Se_{0.07}$. We confirmed the effectiveness of selenium as a solid-solution hardening agent in the CdZnTe matrix. This counters the large thermal stress associated with the higher temperature growth process experienced for ingots grown by the Bridgman method, as compared to THM, and provides the first X-ray topography data on Bridgman-grown CdZnTeSe crystals.

2. Experimental

CdZnTeSe crystals with a nominal concentration of 10% Zn and 7% Se were grown by the vertical Bridgman growth technique. The $Cd_{0.9}Zn_{0.1}Te_{0.93}Se_{0.07}$ compound was synthesized from stoichiometric amounts of 6N purity $Cd_{0.9}Zn_{0.1}Te$ (from 5N Plus, Inc.) and 6N purity CdSe (from Azelis, Inc.) In order to avoid any unwanted impurities, the synthesis and growth were carried out in the same ampoule. Un-seeded ingots were grown in a conically tipped quartz ampoule with the inner and outer diameter of 40 mm and 46 mm, respectively. Prior to loading, the inner wall of the ampoule was coated with carbon by cracking spectroscopic-grade acetone at about 900 ^{0}C. After coating, the ampoule was annealed under vacuum at about 1150 ^{0}C for an hour. The loaded ampoule was then sealed under a dynamic vacuum of ~$2x10^{-6}$ torr. The synthesis and growth were carried out in a three-zone vertical muffle furnace. The ampoule was mounted inside the furnace, and the furnace temperature was raised to about 900 ^{0}C over 24 hours, followed by further raising the temperature to 1130 ^{0}C near the tip at a rate of 4 ^{0}C/hr. To ensure the complete synthesis, the melt was soaked for about 72 hours before commencing the growth.

The ingot was grown with a lowering speed of ~2.5 cm/day, and after completion of the growth, the temperature of the furnace was lowered down to room temperature at a rate of 4 ^{0}C/hr.

The grown ingot was taken out from the ampoule without any sticking to the ampoule wall due to the carbon coating. Wafers of different thicknesses were cut from the ingot perpendicular to the ingot axis using a diamond-impregnated wire saw. To remove the damage caused by the saw, both sides of the wafers were lapped with SiC paper of different grit sizes followed by polishing successively with 3 µm, 1 µm, 0.5 µm and 0.05 µm alumina suspension on felt pads to obtain a mirror-finish surface. To study the presence of extended defects such as sub-grain boundaries and their network, wafers from different portions of the ingot were characterized by White Beam X-ray Diffraction Topography (WBXDT) experiments in the reflection mode using LBNL's Advanced Light Source (ALS) Beamline 3.3.2 with a beam energy ranging from 4 to 25 keV. The details of the X-ray topography measurements are described elsewhere [21]. Prior to the X-ray topographic experiments, polished samples were etched in 2% bromine-methanol solution for two minutes to remove surface damage from the polishing.

3. Results and discussion

A photograph of the Bridgman-grown $Cd_{0.9}Zn_{0.1}Te_{0.93}Se_{0.07}$ ingot is shown in Fig. 1. The grown ingot is 40-mm diameter and about 11 cm in length. The compositional analysis was executed using a JEOL 6500F electron microscope equipped with Energy Dispersive X-ray Analysis (EDAX). The composition near the middle of the ingot was found to be $Cd_{0.91}Zn_{0.89}Te_{0.93}Se_{0.067}$ and agrees well with the nominal concentrations. Figure 2 shows the wafers cut perpendicular to the ingot axis. As is evident from Fig. 2, the ingot is bi-crystal with one very large grain. With the exclusion of the conical part, more than 85-90% of the ingot is single crystalline. It is to be noted that few twins are visible near the conical part of the ingot,

and most of the ingot is twin free. Grain 1, indicated in Fig. 2 by the ellipse, was found to continue towards the end of the ingot, suggesting steady progress of the growth interface. No nucleation from the crucible wall was evident in the grown ingot.

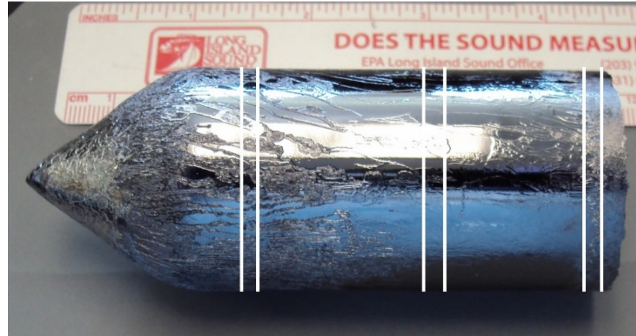

Fig. 1. Optical photograph of the 4-cm diameter $Cd_{0.9}Zn_{0.1}Te_{0.93}Se_{0.07}$ ingot grown by the vertical Bridgman technique. The vertical lines indicate the positions of the wafers used for topographic experiments. (The vertical marks are not drawn to the scale).

Since the X-ray topography technique is very sensitive to the surface quality, especially in the reflection mode, care was taken to remove the damaged layer introduced during the process of

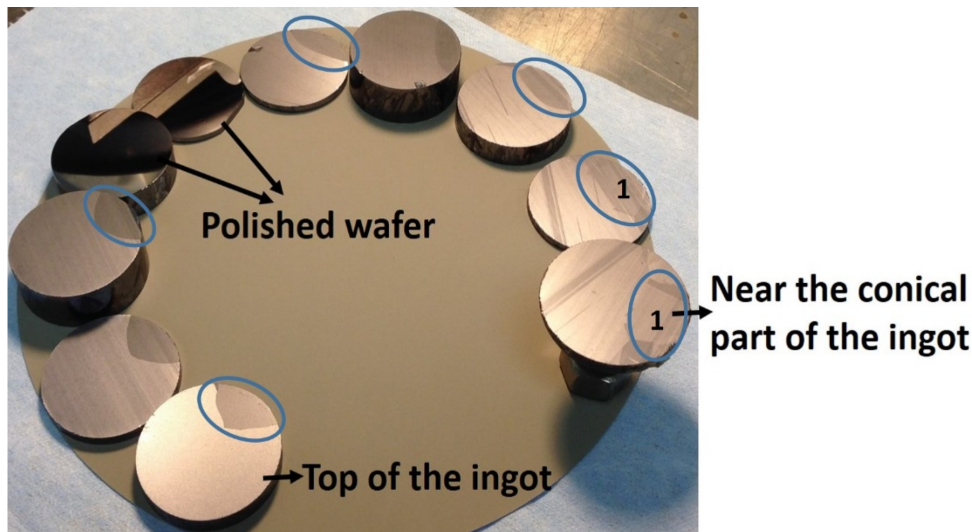

Fig. 2. Optical photograph of the wafers cut perpendicular to the ingot axis.

lapping and polishing of the wafers. All the wafers were polished to flat mirror-like finish using a South Bay Technology Model #920 polishing machine with successive grit sizes and finally

polished with successive alumina suspension on felt pads. All the wafers investigated for X-ray topographic analyses were polished to mirror finish, and subsequently etched in a 2% bromine-methanol solution for two minutes to remove the surface damaged layer prior to the experiments. Figure 3 shows the photograph of a typical polished wafer.

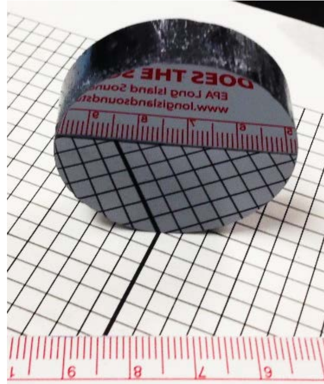

Figure 3. Photograph of a typical 4-cm diameter $Cd_{0.9}Zn_{0.1}Te_{0.93}Se_{0.07}$ polished wafer.

X-ray topographic analyses were carried out for three different wafers taken from top, middle and bottom part of the ingot as indicated in Fig. 1. As mentioned earlier, the X-ray topographic experiments were carried out with a highly polished followed by BM etched surfaces; lapped wafers are shown in the pictures to illustrate the grains and twins present in the wafers.
Fig. 4a shows a photograph of the lapped wafer at the very top surface of the ingot and the corresponding X-ray topographic images. The wafer was cut from the top of the ingot and barely lapped to a flat surface in order to investigate the X-ray topographic characteristics of the top-most part of the ingot. The top of the ingot experienced the maximum thermal stress since this part of the ingot remained at the highest temperature for the longest amount of time. Fig. 4b shows the opposite face of the same wafer with a thickness of ~6.3 mm and the corresponding X-ray topographic image of the region denoted by the white rectangle.

The X-ray topographic image of the region "a" denoted by the white rectangle shows slight lattice distortion near the periphery of the wafer, where the ingot was in touch with the ampoule

wall. However, the streaks near the periphery of the grain “b” in the X-ray topographic image illustrate the presence of high lattice distortion for the region contacting the ampoule wall. Severe lattice distortion resulting from strain introduced by the crucible wall is very common for CdTe and CZT [26-28]. Lattice distortions demonstrated by the streaky nature of the X-ray topographic images near the periphery of the wafers were also observed for contact-less

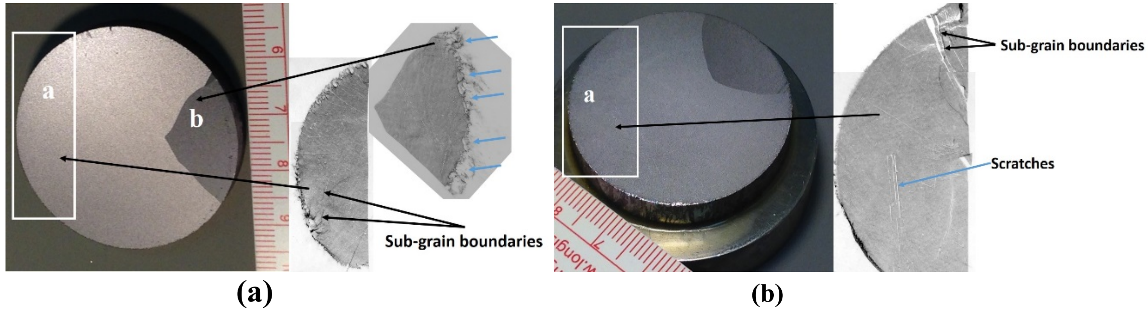

Figure 4. a) Photograph of the 4-cm diameter $Cd_{0.9}Zn_{0.1}Te_{0.93}Se_{0.07}$ lapped wafer cut from the very top of the ingot and the X-ray topographic images of the region denoted by the white rectangle and the grain on the right side of the wafer and b) photograph of bottom part of the wafer and the corresponding X-ray topographic image of the region denoted by the white rectangle (The white rectangles and the corresponding X-ray topographic images are not to scale). Thickness of the wafer: 6.3 mm.

vapor grown CdTe and CZT [27, 28]. The distortion near the periphery for the contact less wafer, was reported to be possible turbulence in the vapor flow pattern near to the wafer edge [28]. Note that, except for the periphery of the grain “b”, the shape of the grain in the topographic image is unaltered. This indicates the absence of overall thermal stress in the wafer. X-ray topographic image displays slight bending of crystal planes caused by internal stresses [11]. Figure 4b shows the opposite face of the same wafer, which is about 6.3 mm from the top of the ingot. No severe lattice distortion near the periphery of the wafer was observed in the X-ray topographic image. In general, X-ray topographic images in reflection mode reveal the presence of sub-grain boundaries as the appearance of white and dark lines based on the tilt angle of adjacent sub-grains. The white and dark lines appear due to the separated and overlapping diffracted images of adjacent sub-grains respectively, due to the tilt angle of the adjacent sub-

grains [21]. The dark lines can also appear due to the possible cracks present in the sample. However, from high magnification IR transmission microscopic analyses (magnification 2.5x to 50x), we did not observe any crack present in the samples [25, 29]. The X-ray topographic images for both sides of the top wafer revealed the presence of very few sub-grain boundaries and the absence of a sub-grain boundary network. Figure 5 shows the lapped wafer section from the middle of the ingot and the corresponding X-ray topographic image of region "a". The X-ray topographic image revealed the presence of few sub-grain boundaries, and no major lattice distortion was observed at the periphery of the wafer.

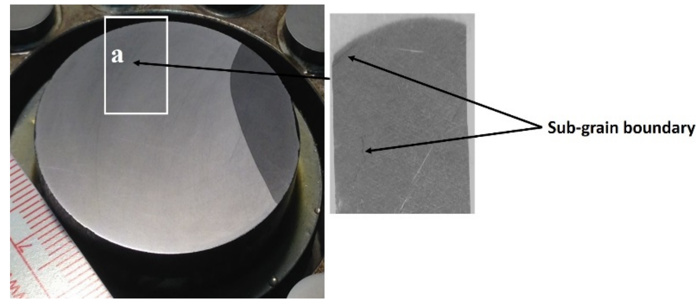

Figure 5. Photograph of the 4-cm diameter $Cd_{0.9}Zn_{0.1}Te_{0.93}Se_{0.07}$ lapped wafer cut near the middle of the ingot and the X-ray topographic image of the region denoted by the white rectangle. (The white rectangle and the corresponding X-ray topographic images are not to scale).

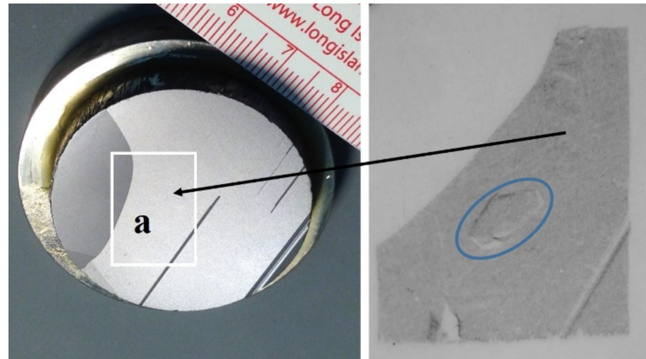

Figure 6. Photograph of the 4-cm diameter $Cd_{0.9}Zn_{0.1}Te_{0.93}Se_{0.07}$ lapped wafer cut from bottom of the ingot and the X-ray topographic image of the region denoted by the white rectangle. (The white rectangle and the corresponding X-ray topographic images are not to scale).

The wafer cut from the bottom of the ingot (just above the conical part of the ingot) and the corresponding X-ray topographic image are illustrated in Fig. 6. The straight nature of the twin in the topographic image represents the fact that the wafer is stress free. The defect indicated inside the blue ellipse in the topographic image is possibly a sub-grain boundary in a closed loop.

Overall, the circular nature of the periphery of the wafers and the grain boundaries were not observed to be deformed substantially in the topographic images, which implies the absence of thermal stress in the wafers. The circular characteristic has previously been observed to be deformed due to lattice distortion/defects for contact-less CZT wafers grown by the Multi-Tube Physical Vapor Transport (MTPVT) method [28]. The striking feature of all the topographic images from different part of the CZTS ingot grown for this study is the absence of a sub-grain boundary network, despite slight segregation of Zn along the growth direction. The Zn concentrations were observed to be ~ 9.8, 8.9 and 7.9 atomic% for near the bottom, middle and near the top of the ingot and measured by EDAX. This is consistent with our previous observation for THM-grown CdTeSe and CZTS [21, 23-25]. The addition of selenium in the CZT matrix proved to be an effective solution-hardening element in producing Bridgman-grown CZTS ingots, as well as THM-grown ingots, that are stress-free and possess no sub-grain boundary network for various compositions with Se ranging from 1.5% to 7% [23-25, 29]. This is a significant material improvement with important implications for gamma-ray detector applications, as the current state-of-the-art material (CZT) generally contains extended sub-grain boundary networks [11].

4. Summary:

We have characterized the crystalline quality of CZTS grown by the vertical Bridgman growth technique by X-ray topography in the reflection mode using a synchrotron source. The X-ray

topographic experiments were performed on wafers from the top, middle and bottom parts of the grown ingot. The topographic study revealed that the CZTS ingot is relatively free of strain, even in the periphery of those wafers that were in contact with the ampoule wall. Very few sub-grain boundaries were observed, and the entire ingot was found to be free from a sub-grain boundary network, confirming that selenium is an effective solid-solution hardening component in the CZT matrix.

Acknowledgements:

This work was supported primarily by the U.S. Department of Energy, Office of Defense Nuclear Nonproliferation Research and Development, DNN R&D. The manuscript has been authored by Brookhaven Science Associates, LLC under Contract No. DE-SC0012704 with the U.S. Department of Energy.

References:

1. T. E. Schlesinger, J. E. Toney, H. Yoon, E. Y. Lee, B. A. Brunett, L. Franks, and R. B. James, Mater. Sci. Eng. R **32** (2001) 103.

2. G. Yang and R. B. James, in Physics, Defects, Hetero- and Nano-Structures, Crystal Growth, Surfaces and Applications: Part II, EDAX, edited by R. Triboulet et al. (Elsevier, 2009), p. 214.

3. U. N. Roy, A. Burger, and R. B. James, J. Cryst. Growth **379** (2013) 57.

4. J. S. Lee, G. Kovalski, T. Sharir and D. S. Lee, J. Nuclear Cardiology **26** (2019) 543.

5. H. Chen, H. Li, M. D. Reed, A. G. Sundaram, J. Eger, J. W. Hugg, S. Abbaszadeh, M. Li, G. Montemont, L. Verger, Y. Zhu, Z. He, Proc. of SPIE **10762**, (2019) N-1.

6. L. Marchini, A. Zappettini, M. Zha, N. Zambelli, A. E. Bolotnikov, G. S. Camarda, and R. B. James, IEEE Trans. Nucl. Sci. **59** (2012) 264.

7. A. Hossain, A. E. Bolotnikov, G. S. Camarda, Y. Cui, G. Yang, K-H. Kim, R. Gul, L. Xu, and R. B. James, J. Cryst. Growth **312** (2010) 1795.

8. A. Hossain, A. E. Bolotnikov, G. S. Camarda, Y. Cui, R. Gul, U. N. Roy, G. Yang, and R. B. James, J. Cryst. Growth **470** (2017) 99.

9. A. E. Bolotnikov, S. Babalola, G. S. Camarda, Y. Cui, R. Gul, S. U. Egarievwe, P. M. Fochuk, M. Fuerstnau, J. Horace, A. Hossain, F. Jones, K. H. Kim, O. V. Kopach, B. McCall, L. Marchini, B. Raghothamachar, R. Taggart, G. Yang, L. Xu, and R. B. James, IEEE Trans. Nucl. Sci. **58** (2011) 1972.

10. A. E. Bolotnikov, N. M. Abdul-Jabbar, O. S. Babalola, G. S. Camarda, Y. Cui, A. M. Hossain, E. M. Jackson, H.C. Jackson, J. A. James, K. T. Kohman, A. L. Luryi, and R. B. James, IEEE Trans. Nucl. Sci. **55** (2008) 2757.

11. A. E. Bolotnikov, G. S. Camarda, Y. Cui, G. Yang, A. Hossain, K. Kim, and R. B. James, *J. Cryst. Growth* **379** (2013) 46.

12. D. Zeng, W. Jie, T. Wang, and H. Zhou, J. Cryst. Growth **311** (2009) 4414.

13. A.E. Bolotnikov, S.O. Babalola, G.S. Camarda, H. Chen, S. Awadalla, Y. Cui, S.U. Egarievwe, P.M. Fochuk, R. Hawrami, A. Hossain, J.R. James, I.J. Nakonechnyj, J. Mackenzie, G. Yang, C. Xu, and R.B. James, IEEE Trans. Nucl. Sci. **56** (2009) 1775.

14. G. A. Carini, A. E. Bolotnikov, G. S. Camarda and R. B. James, Nucl. Instrum. Methods **A 579** (2007) 120.

15. M. Amman, J. S. Lee, and P. N. Luke, J. Appl. Phys. **92** (2002) 3198.

16. G. Yang, A. E. Bolotnikov, P. M. Fochuk, O. Kopach, J. Franc, E. Belas, K. H. Kim, G. S. Camarda, A. Hossain, Y. Cui, A. L. Adams, A. Radja, R. Pinder, and R. B. James, J. Cryst. Growth **379** (2013) 16.

17. A. E. Bolotnikov, G. S. Camarda, E. Chen, S. Cheng, Y. Cui, R. Gul, R. Gallagher, V. Dedic, G. De Geronimo, L. Ocampo Giraldo, J. Fried, A. Hossain, J. M. MacKenzie, P. Sellin, S. Taherion, E. Vernon, G. Yang, U. El-Hanany, and R. B. James, Appl. Phys. Lett. **108** (2016) 093504.

18. P. Rudolph, Prog. Cryst. Growth and Characterization of Materials **29** (1994) 275.

19. A. Tanaka, Y. Masa, S. Seto, and T. Kawasaki, J. Cryst. Growth **94** (1989) 166.

20. U. N. Roy, A. E. Bolotnikov, G. S. Camarda, Y. Cui, A. Hossain, K. Lee, M. Marshall, G. Yang, and R. B. James, J. Cryst. Growth **386** (2014) 43.

21. U. N. Roy, A. E. Bolotnikov, G. S. Camarda, Y. Cui, A. Hossain, K. Lee, G. Yang, and R. B. James, J. Cryst. Growth **389** (2014) 99.

22. M. Fiederle, D. Ebling, C. Eiche, D.M. Hofmann, M. Salk, W. Stadler, K. W. Benz, and B. K. Meyer, J. Cryst. Growth **138** (1994) 529.

23. U. N. Roy, G. S. Camarda, Y. Cui, R. Gul, A. Hossain, G. Yang, J. Zazvorka, V. Dedic, J. Franc and R. B. James, Scientific Reports **9** (2019) 1620.

24. U.N. Roy, G. S. Camarda, Y. Cui, R. Gul, G. Yang, J. Zazvorka, V. Dedic, J. Franc and R.B. James, Scientific Reports **9** (2019) 7303.

25. U.N. Roy, G.S. Camarda, Y. Cui, and R.B. James, Appl. Phys. Lett. **114** (2019) 232107.

26. C. H. Su, S. L. Lehoczky, B. Raghothamachar, and M. Dudley, Mat. Sc. and Engr. **B 147** (2008) 35.

27. W. Palosz, K. Grasza, K. Durose, D.P. Halliday, N.M. Boyall, M. Dudley, B. Raghothamachar, and L. Cai, J. Cryst. Growth **254** (2003) 316.

28. C.K. Egan, A. Choubey, M. Moore and R. Cernik, J. Cryst. Growth **343** (2012) 1.

29. U.N. Roy, G.S. Camarda, and R.B. James, Appl. Phys. Lett. **115** (2019) 242102.

Captions to the figures:

Fig. 1. Optical photograph of the 4-cm diameter $Cd_{0.9}Zn_{0.1}Te_{0.93}Se_{0.07}$ ingot grown by the vertical Bridgman technique. The vertical lines indicate the positions of the wafers used for topographic experiments. . (The vertical marks are not drawn to the scale).

Fig. 2. Optical photograph of the wafers cut perpendicular to the ingot axis.

Figure 3. Photograph of a typical 4-cm diameter $Cd_{0.9}Zn_{0.1}Te_{0.93}Se_{0.07}$ polished wafer.

Figure 4. a) Photograph of the 4-cm diameter $Cd_{0.9}Zn_{0.1}Te_{0.93}Se_{0.07}$ lapped wafer cut from the very top of the ingot and the X-ray topographic images of the region denoted by the white rectangle and the grain on the right side of the wafer and b) photograph of bottom part of the wafer and the corresponding X-ray topographic image of the region denoted by the white rectangle (The white rectangles and the corresponding X-ray topographic images are not to scale). Thickness of the wafer: 6.3 mm.

Figure 5. Photograph of the 4-cm diameter $Cd_{0.9}Zn_{0.1}Te_{0.93}Se_{0.07}$ lapped wafer cut near the middle of the ingot and the X-ray topographic image of the region denoted by the white rectangle. (The white rectangle and the corresponding X-ray topographic images are not to scale).

Figure 6. Photograph of the 4-cm diameter $Cd_{0.9}Zn_{0.1}Te_{0.93}Se_{0.07}$ lapped wafer cut from bottom of the ingot and the X-ray topographic image of the region denoted by the white rectangle. (The white rectangle and the corresponding X-ray topographic images are not to scale).